Dopant induced hollow Ni$_2$P nanocrystals regulate dehydrogenation kinetics for highly efficient solar-driven hydrazine assisted H$_2$ production

Umesh P. Suryawanshi [a], Uma V. Ghorpade [b], Priyank V. Kumar [b], Jun Sung Jang [a], Mingrui He [c], Hong Jae Shim [c], Hyo Rim Jung [a], Mahesh P. Suryawanshi [c,*], Jin Hyeok Kim [a,*]

[a] *Optoelectronics Convergence Research Center and Department of Materials Science and Engineering, Chonnam National University, 300, Yongbong-Dong, Buk-Gu, Gwangju 61186, South Korea*
[b] *School of Chemical Engineering, University of New South Wales, Sydney, NSW 2052 Australia*
[c] *School of Photovoltaic and Renewable Energy Engineering, University of New South Wales, Sydney, NSW 2052, Australia*

ABSTRACT

Replacing kinetically sluggish oxygen evolution reaction (OER) with a thermodynamically favorable hydrazine oxidation reaction (HzOR) to produce hydrogen has emerged as a more energy-efficient alternative than water splitting. However, the lack of promising bifunctional electrocatalysts hinders its scalable applications. Here, we report a colloidal synthesis of Mn-dopant induced hollow Ni$_2$P nanocrystals (NCs) using a heat-up approach, which act as superior bifunctional electrocatalysts for both HzOR (55 mV at 10 mA/cm^2) and hydrogen evolution reaction (HER, 192 mV at 50 mA/cm^2). The two-electrode electrolyzer requires a low cell voltage of 59 mV to achieve 10 mA/cm^2 and a current density of ~ 50.4 mA/cm^2 to reach 0.5 V. Theoretical studies unraveled that Mn-doping regulates the electronic structure of Ni$_2$P and optimizes the H* adsorption/desorption and dehydrogenation kinetics. When integrated with a Si photovoltaic device, the bifunctional hollow Mn-doped Ni$_2$P NCs enabled solar-driven hydrazine assisted H$_2$ production with a ~ 14.6 % efficiency.

1. Introduction

Hydrogen (H$_2$), an ideal energy carrier, produced through the water electrolysis has been considered as one of the most riveting alternatives to replace the contemporary fossil fuel energy framework [1]. H$_2$ production by electrochemical water splitting involves two half reactions, namely hydrogen evolution reaction (HER) and oxygen evolution reaction (OER). Regardless of considerable progress, sadly, the cathodic HER is highly dependent on sluggish reaction kinetics of anodic OER. Since OER involves four-electron transfer process that not only requires more than 1.40 V to drive the electrolysis process [2], but also increases the cost of electrolyzer, making it highly undesirable for large-scale application [3–5]. Hence, it is significantly desired to discover an alternative strategy to OER, instead of developing high performance OER electrocatalysts that could lower the overall cell voltage and improve the H$_2$ conversion efficiency. In this regard, replacing anodic OER with the electro-oxidation of small molecules with favorable thermodynamic potential have been demonstrated to achieve energy-efficient H$_2$ production at relatively low cell voltages [6–12].

Some early works have proved the notability of hydrazine oxidation reaction (HzOR, N$_2$H$_4$ + 4OH$^-$ → N$_2$ + 4 H$_2$O + 4e$^-$) at anode side for hydrazine-assisted overall water splitting (HzOWS) to produce H$_2$ due to its extremely lower theoretical potential of −0.33 V (vs. reversible hydrogen electrode (RHE)) in contrast with the OER (1.23 V vs. RHE) [13,14]. Notably, HzOWS allows the use of membrane-free electrolyzer as it produces nitrogen (N$_2$) as the only byproduct instead of the explosive H$_2$/O$_2$ mixture in case of overall water splitting (OWS), hence avoiding the major barrier to future large scale practical applications [15,16]. To date, tremendous efforts have been made on the design and development of advanced and low-cost electrocatalysts for HER and OER and some remarkable achievements have been made [17,18]. However, the development of earth-abundant electrocatalysts for HzOR is still in its early stages, not to mention bifunctional electrocatalysts for both HER and HzOR. Several pioneering works have gained spectacular breakthroughs in this regard [14,19,20]. For example, Sun and co-workers [14] first demonstrated that the high HER catalytic activity of Ni$_2$P could acts as a bifunctional catalyst for H$_2$ generation with HzOR replacing OER. They reported that Ni$_2$P nanoarrays in-situ grown on Ni

---

* Corresponding authors.
E-mail addresses: m.suryawanshi@unsw.edu.au (M.P. Suryawanshi), jinhyeok@chonaam.ac.kr (J.H. Kim).

foam showed a superior catalytic activity with a cell voltage of 1.0 V at 500 mA/cm^2. Mai and co-workers [21] reported a new type of bimetallic copper–nickel nitride (Cu$_1$Ni$_2$-N) with nickel nitride/copper nitride interface developed on carbon fiber cloth exhibited an excellent electrocatalytic activity for HzOWS with a cell voltage of 0.24 V at 10 mA/cm^2. Rh$_2$P ultrathin nanosheets with atomic thickness and large surface area synthesized by Chen's group act as a bifunctional HER and HzOR electrocatalyst, which required a cell voltage of 0.164 V to achieve current density of 10 mA/cm^2 for HzOWS [22]. In notable work, Zhang and co-workers [23] demonstrated that the partially exposed RuP$_2$ nanoparticles-decorated with porous carbon microsheets outperform Pt/C electrocatalysts for both HER and HzOR and showed a record-low cell voltage of 0.023 V at 10 mA/cm^2 for HzOWS in a two-electrode system. In spite of enlightened pioneering works, the obstacles of reducing cell voltages in two electrode systems, especially at high current densities, remain, necessitating a smart and precise strategies to design new electrocatalysts with exceptional performance towards both HER and HzOR. This undoubtedly demands theoretical investigation into the underlying fundamental mechanisms of new electrocatalysts for HzOR.

Colloidal nanocrystals (NCs) of transition metal phosphides (TMPs) have received extraordinary attention as efficient electrocatalysts for HER in recent years due to their low-cost, outstanding activity and physio-chemical stability [24–28]. It has been demonstrated that the electrocatalytic performance of NCs can be enhanced by controlling their size, shape, and composition [29,30]. One possible strategy is to reduce the size of NCs to greatly increase active sites; nevertheless, severe aggregation of NCs at a narrow size distribution, which impedes mass diffusion and electrocatalytic activity, is still unavoidable. The incorporation of foreign transition metals into TMPs have been suggested to tune the intrinsic activity by improving their coordination environment of electrons/active surface sites [31,32]. Another promising approach is hollow NCs with high surface-to-volume ratio and good penetrability, which provide an efficient channel for mass/charge diffusion while also providing additional surface-active sites, have been employed as effective electrocatalysts for HER, OER, and oxygen reduction reactions [33–35]. To date, most of hollow TMP NCs have been primarily prepared by template-assisted approaches [36,37], which may be difficult to extend to the parathion of bimetallic hollow TMP NCs. There is still a grand challenge for the preparation of bimetallic hollow TMP NCs with small narrow size distribution. As a consequence, it is reasonable to decipher that designing a bimetallic hollow TMPs NCs with narrow size distribution that act as a bifunctional electrocatalysts for HER and HzOR, which has not been yet reported in the literature.

Here, we demonstrate a colloidal synthesis of hollow Mn-doped Ni$_2$P (denoted as Ni$_{2-x}$Mn$_x$P) NCs as a result of Kirkendall effect using a heat-up approach that act as a bifunctional electrocatalysts for both HzOR and HER. Remarkably, as-prepared Ni$_{2-x}$Mn$_x$P (x = 0.6) electrocatalyst achieved current density of 10 and 50 mA/cm^2 with required working potential of 55 mV and 151 mV (vs. RHE), respectively for HzOR in 1 M KOH/0.5 M hydrazine electrolyte. Notably, Ni$_{2-x}$Mn$_x$P (x = 0.6) electrocatalyst also showed a low overpotential of 192 mV at 50 mA/cm^2 for HER with Tafel slope of 48 mV.dec^{-1}, as well as stability over 20 h in 1 M KOH. Impressively, a low cell voltage of 59 mV is required to achieve 10 mA/cm^2 in a two-electrode system for HzOWS, and reached current density of ∼ 50.4 mA/cm^2 at a cell voltage of only 0.5 V. The density functional theory (DFT) calculations decipher that the Mn doping in Ni$_2$P not only decreases the free-energy changes of the dehydrogenation of adsorbed NH$_2$NH$_2$ (denoted as *NH$_2$NH$_2$), but also make the free energy of adsorbed H (ΔG_{H*}) more thermoneutral compared to pristine Ni$_2$P. Furthermore, we demonstrated the potential applications of Ni$_{2-x}$Mn$_x$P (x = 0.6) electrocatalyst in solar-driven HzOWS by coupling with a commercial Si photovoltaic (PV) device, which generated a stable photocurrent density of ∼ 12.1 mA/cm^2 with a solar-to-hydrogen (STH) efficiency of ∼ 14.6 %.

2. Experimental

2.1. Chemicals and materials

Nickel (II) acetate tetrahydrate (Ni(CH$_3$CO$_2$)$_2$·4 H$_2$O, Ni(acac)$_2$), manganese(II) acetate tetrahydrate (Mn(CH$_3$COO)$_2$·4 H$_2$O, Mn(acac)$_2$), nickel (II) chloride hexahydrate (NiCl$_2$·6 H$_2$O), manganese (II) chloride hydrate (MnCl$_2$.4 H$_2$O), 1-octadecene (ODE), oleylamine (OLA) and tri-n-octylphosphine (TOP), *n*-Hexane, ethanol, toulene, hydrazine hydrate (N$_2$H$_4$·xH$_2$O, 50–60 wt%) and 5 wt% Nafion solution were purchased from Sigma Aldrich. All of the chemicals were used as receive without any further purification.

2.2. Synthesis of solid Ni$_2$P and hollow Ni$_{2-x}$Mn$_x$P NCs

In a typical synthesis, Ni(acac)$_2$ (1, 0.9, 0.8 and 0.7 mmol) and Mn (acac)$_2$ (0, 0.1, 0.2 and 0.3 mmol) was added to a 100-mL three-necked, round bottom flask containing a borosilicate stir bar and equipped with thermocouple and rubber septum. Prior to sealing the flask, 1-ODE (9.4 mmol), OLA (13 mmol), and TOP (8.99 mmol) were added to the vessel. The reaction mixture was moderately stirred and heated, using a heating mantle, at 120 °C for 1 h under vacuum, to remove water and other low-boiling impurities. The solution was then heated at 320 °C for 4 h in an Ar atmosphere. After holding the solution at above mentioned parameters, the reaction was cooled slowly by turning off the heating mantle until the solution reached 200 °C. The flask was then removed from the heating mantle to effect rapid cooling to room temperature. The contents of the reaction mixture were transferred into centrifuge tubes equipped with caps, followed by centrifugation at 6000 rpm for 10 min. The resultant NCs was washed 3 times using 1:3 (V:V) hexane: ethanol and then was dispersed in *n*-hexane for further use. To synthesize solid Ni$_2$P NCs, similar reaction process was followed except the addition of manganese precursor into reaction bath and keeping all other reaction conditions and purification steps same.

2.3. Materials characterizations

The surface morphologies were studied using high-resolution Transmission electron microscopy (HR-TEM, JEOL-3010) with an accelerating voltage of 300 kV located at Korea Institute of Basic Sciences (KBSI), Gwangju, South Korea. Ni$_{2-x}$Mn$_x$P NCs, dispersed in toluene, are drop casted onto carbon meshed nickel grid for TEM sampling. The elemental distribution and compositional information were investigated by energy dispersive X-ray spectroscopy (EDS, OXFORD INCA system) using A Technai G2 F30 equipped with FE-SEM. The structural properties of the material were analyzed by the X-ray diffraction (XRD), using a XRD, PANalytical, X'Pert-PRO Netherland operated at 45 kV, 40 mA, and room temperature. A high-resolution X-ray photoelectron spectroscopy (HR-XPS, VG Multi lab 2000, Thermo VG Scientific, UK) at room temperature. The binding energy is calibrated to C 1 s, 285.0 eV.The EXAFS of Ni k-edge and Mn k-edge were collected on the Rigaku X-ray Absorption Spectrometer (R-XAS) in Leaders in Industry-University Corporation (LINC), Gwangju, South Korea.

2.4. Electrochemical characterizations

All electrochemical performances of the samples were evaluated by using an Autolab potentiostat (CHI Instruments, USA) at room temperature. In a conventional three electrode system, the as-prepared electrocatalysts were used as a working electrode with the graphite rod as a counter electrode and saturated Ag/AgCl in 3.5 M KCl (0.209 V vs. NHE) was used as the reference electrode. To prepare the working electrode, 10 mg of catalysts, 50 μL of Nafion solutions were dispersed in toluene (5 mL) followed by ultrasonication for at least 2 h to form homogeneous catalyst ink. Then the catalyst ink was loaded on Ni foam with a mass loading of 5 mg/cm. An aqueous electrolyte containing 1.0 M KOH (pH

= 14) was used for the HER and 1.0 M KOH/0.5 M hydrazine was used for HzOR electrochemical measurements. Prior to the measurement, the aqueous electrolyte was treated with N_2 for 30 min. to remove the dissolved oxygen (O_2) species in the solution. All the potentials reported were converted with respect to a reversible hydrogen electrode (RHE) using the following standard Nernst equation.

$$E_{RHE} = E_{Ag/AgCl} + 0.05916 \times pH + E° \tag{1}$$

where, E_{RHE} is the potential vs. RHE, $E_{Ag/AgCl}$ is the potential measured vs. Ag/AgCl and $E°_{Ag/AgCl} = 0.198$ V at room temperature.

Linear sweep voltammetry (LSV) curves were recorded at different scan rate (5, 10, 20, 40, 60 and 80 mV s^{-1}). Electrochemical impedance spectroscopy (EIS) was performed in same electrochemical configuration and electrolyte under the dark condition on an Autolab PGSTAT equipped with an FRA2 frequency response analyzer with Nova 1.7 controlled data acquisition under open-circuit voltage. The EIS measurements were carried out in potentiostat mode at open circuit potential in the frequency range from 0.1 Hz to 10 kHz with an amplitude of ± 10 mV. Each EIS spectrum were modeled using the suggested equivalent circuit by using the Z view program with relative errors below 5 %. Cyclic voltammograms (CVs) were recorded at different scan rates (5, 10, 15, 20, 25 mV s^{-1}) to estimate the double-layer capacitance (C_{dl}). A chronopotentiometric measurements were conducted to test the stability of $Ni_{2-x}Mn_xP$ NCs electrocatalysts at constant current density of 10 mA/cm^2 and in a fixed potential window, respectively.

2.5. Computational details

The VASP code was used for all our DFT calculations [38,39]. The core electrons were treated using the projector augmented wave method (PAW) method [40], and the Perdew-Burke-Ernzerhof (PBE)

exchange-correlation functional was used [41]. The kinetic energy cut-off for the wavefunctions was 500 eV. All relaxations proceeded until the residual forces on atoms were less than 0.03 eV/Å. A vacuum region greater than 10 Å in the surface normal direction to avoid interaction between the images. A 2×2 Ni_2P (001) super cell (surface dimensions of 11.75 Å × 11.75 Å) was employed to model hydrogen evolution and hydrazine reduction reactions. The Mn-doped structure was modeled by replacing one, two and three Ni atoms in the sub-surface layer by one, two and three Mn atoms to create 1Mn, 2Mn and 3Mn-doped structures as mentioned in the main text. The free energy changes upon adsorption were computed using the computational hydrogen electrode (CHE) approach [42,43], where the free energy of $(H^+ +e^-)$ equals $\frac{1}{2}H_2(g)$ for a standard hydrogen electrode (SHE). The free energy of various intermediates is calculated as:

$$G = E_{elec} + E_{ZPE} - TS \tag{2}$$

where, E_{elec} is the total electronic energy computed by DFT; E_{ZPE} is the zero-point energy (ZPE), T is temperature and S is entropy. For H adsorption, the change in free energy is computed as $\Delta G = \Delta E_{elec} + 0.24$ eV. For modeling the hydrazine reduction reaction, we only considered the total electronic energy term and neglected additional corrections.

3. Results and discussion

3.1. Synthesis and characterizations of hollow $Ni_{2-x}Mn_xP$ NCs

Although the synthesis of colloidal $Ni_{2-x}Mn_xP$ NCs has been reported [44], in-depth studies on the synthesis of hollow NCs with varied composition ratios have yet to be conducted. Moreover, insights into the synthesis mechanism of Mn-dopant induced hollow Ni_2P NCs have not been explored. The hollow $Ni_{2-x}Mn_xP$ NCs were synthesized using a
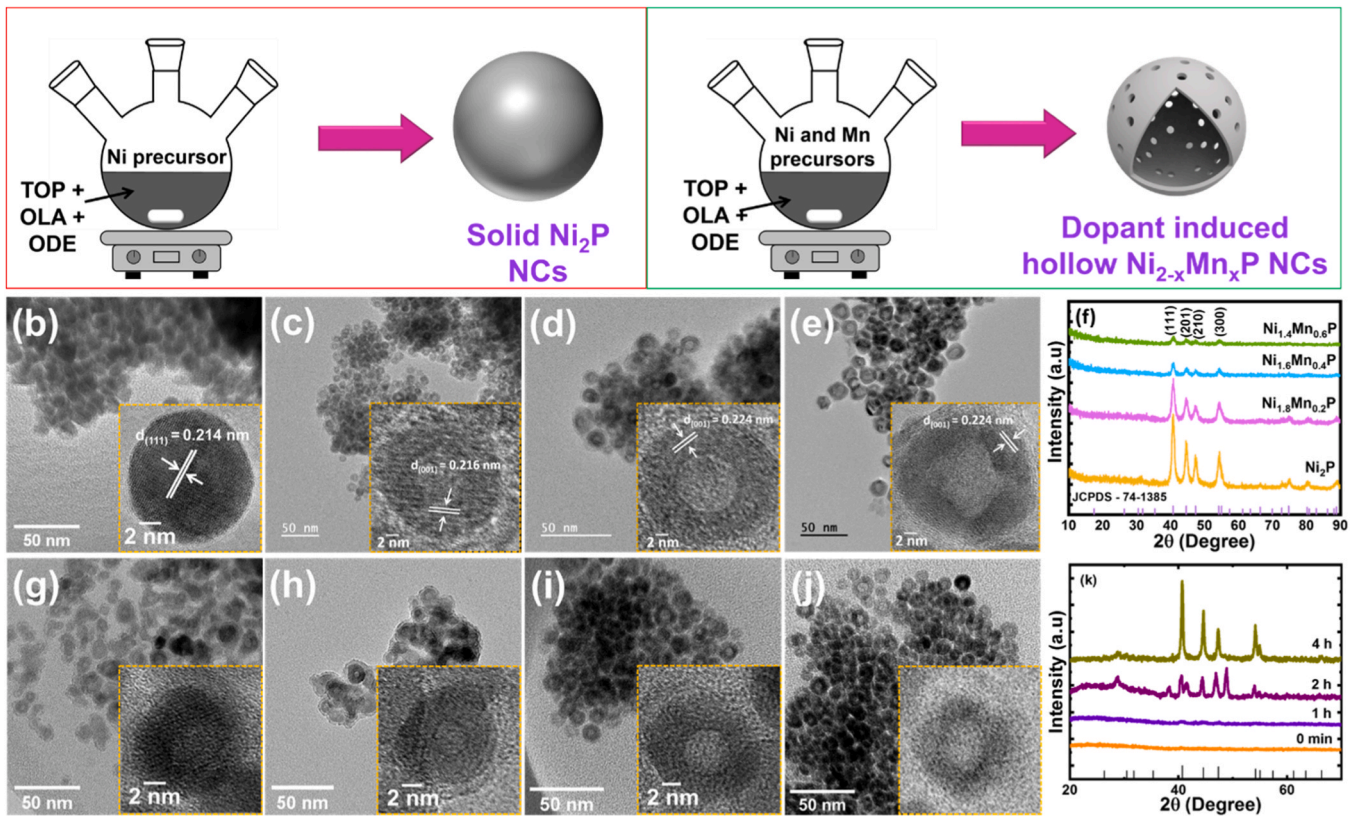

Fig. 1. (a) Schematic illustration of synthesis processes of solid Ni_2P (left red panel) and hollow $Ni_{2-x}Mn_xP$ NCs (right green panel). (b) TEM and HR-TEM (inset) images of Ni_2P NCs. (c-e) TEM and HR-TEM (inset) images, and (f) XRD patterns of $Ni_{2-x}Mn_xP$ NCs with different Mn composition (x = 0, 0.2, 0.4, and 0.6). (g-j) TEM and HR-TEM (inset) images of NC hollowing process at different reaction times (0 min., 1 h, 2 h, and 4 h), and k) their corresponding XRD patterns.

simple and scalable heat-up approach. Ni(acac)$_2$ and Mn(acac)$_2$ were chosen as the metal sources, trioctylphosphine (TOP) as a phosphorous source, and 1-octadecane (ODE) and oleylamine (OAm) as the solvents. Fig. 1**a** illustrate the schematic representation of the synthesis process. By directly heating Ni(acac)$_2$ solution with TOP, spherical Ni$_2$P NCs with an average size of $\sim 12 \pm 2$ nm were obtained (Fig. 1**b**). The crystalline Ni$_2$P NCs show clearly visible lattice fringes with the d-spacing of 0.214 nm, which corresponds to (001) plane of hexagonal Ni$_2$P (Fig. 1**b, inset**). More interestingly, when Mn(acac)$_2$ was added together with Ni (acac)$_2$ and TOP, spherical hollow Ni$_{2-x}$Mn$_x$P NCs were formed, demonstrating the role of Mn in the formation of hollow NCs. Fig. 1**c-e and g-j** shows the high-magnification TEM images of the synthesized hollow Ni$_{2-x}$Mn$_x$P NCs under different reaction conditions. It is well known that moving from monometallic to bimetallic NCs, the different diverse interactions between two metal species along with the solvents impact the quality of final product. Therefore, the optimization of a greater number of reaction parameters is highly necessary to synthesize high-quality Ni$_{2-x}$Mn$_x$P NCs. Optimizing the compositional ratios of Ni and Mn is crucial for directing the synthesis towards Ni$_{2-x}$Mn$_x$P NCs with consistent crystal structures across the whole composition while avoiding the formation of competing undesirable phase. We initially carried out the synthesis of Ni$_{2-x}$Mn$_x$P NCs by varying Ni and Mn precursor contents in the desired ratio of x = 0–1 in the interval of 0.1. Surprisingly, we found that the Ni$_{2-x}$Mn$_x$P NCs can be synthesized with consistent crystal structures (hexagonal structure with space group of $P\bar{6}2m$) only up to 30% Mn incorporation, while more than 30 % Mn incorporation led to the formation of major phase of MnO$_2$ (Fig. S1). This is due to the saturation of solubility limit of Mn in Ni$_2$P system over 30% doping concentration and the highly oxophilic nature of Mn [45]. Intriguingly, we were unable to successfully synthesize the Mn$_2$P phase, often leading to the formation of the MnP phase or no isolable product. Therefore, we focused our further investigation on the Ni$_{2-x}$Mn$_x$P NCs within the composition ratio of x = 0–0.6 in the range of 0.2.

It has been suggested that the hollow NCs formed through a vacancy-mediated diffusion mechanism, in which an outward mass flow of the faster diffusing metal species into a reactive environment is balanced by the opposite flow of vacancies that condense voids into solids [46,47]. Thus, it can be concluded that the diffusion rate of metals in bimetallic phosphides plays a key role in the formation of hollow colloidal NCs. The Kirkendall effect is therefore responsible for the formation of hollow Ni$_{2-x}$Mn$_x$P NCs generated by a vacancy-mediated diffusion process [48]. Transmission Electron Microscopy (TEM) images confirm the formation of hollow NCs after Mn incorporation, as illustrated in Fig. 1**c-e**. The mechanism behind the hollow nanostructure is analogous to the void formation in the Kirkendall effect, in which the diffusion coefficient of the elements in diffusion pair fluctuates significantly [49]. This effect majorly arises from the diffusion couple between Ni and Mn [50]. The TEM images show a relatively uniform spherical morphology for each of the as-synthesized Ni$_{2-x}$Mn$_x$P NCs with the average sizes of 14 ± 3 nm (Ni$_{1.8}$Mn$_{0.2}$P), 15 ± 2.5 nm (Ni$_{1.6}$Mn$_{0.4}$P) and 18 ± 1.8 nm (Ni$_{1.4}$Mn$_{0.6}$P), respectively. The corresponding high resolution TEM images (Fig. 1**c-e, insets**) further revealed that the hollow NCs are crystalline and faceted with lattice d-spacing value of 0.216 nm, 0.224 nm, and 0.236 nm (the distance of (001) planes) for all NCs. These lattice d-spacings slightly varied in the range depending on the alloy composition. Inductively coupled plasma optical emission spectroscopy (ICP-OES) data in Table S1 for Ni$_{2-x}$Mn$_x$P (x = 0, 0.2, 0.4 and 0.6) support the results from energy-dispersive spectroscopy (EDS) (Fig. S2a). The scanning TEM (STEM) and EDS elemental mapping images, which are consistent with the XRD and ICP-OES results, also demonstrate that the Ni, Mn, and P elements are homogeneously distributed throughout hollow NCs (Fig. S2b).

At this stage, it becomes interesting to investigate the formation process of hollow Ni$_{2-x}$Mn$_x$P NCs. To explore this process, the intermediate products obtained at different reactions times were analyzed using

TEM, HR-TEM and XRD. As seen from the TEM images (Fig. 1**g-j**), hollowing of NCs begins and starts to create the vacancies in between reaction times of 1 and 2 h (Fig. 1**h and i**). Furthermore, these vacancies migrate and eventually agglomerate to create smaller voids, which converge into a single larger void during the final conversion phase due to the massive difference in the surface energy between the smaller voids and the single larger void (Fig. 1**j**) [44]. The PXRD patterns (Fig. 1**k**) further decode the phase transformation with respect to reaction time. In the initial stage of the reaction (0 min. and 1 h), poorly crystalline materials with broad peaks were obtained. We note that the products at reaction time of 0 min. and 1 h tend to attract to the stir bar, implying that the conversion of Ni and Mn precursors was incomplete. In subsequent reaction time of 3 h and 4 h, this poorly crystalline product evolved into highly crystalline products with sharp peaks corresponding to the Mn-doped Ni$_{12}$P$_5$ and Ni$_2$P phase, with latter being the dominant phase at a reaction time of 4 h. ICP-OES data further revealed the evolution of Mn content in Ni$_{1.4}$Mn$_{0.6}$P NCs from Mn-rich to Mn-deficient with increase in reaction time (Table S2). Based on the XRD and ICP-OES results, we propose that the Ni could be etched by additional phosphorous in a reactive environment, facilitating formation of corrosion sites. Meanwhile, the vacancies caused by reduced Mn ions would expand into the void, eventually forming a hollow structure. Thus, the Mn-deficient NCs at longer reaction times (2 h and 4 h), eventually formed the hollow NCs due to the sufficient time allowed for the reduction of all Mn ions. In short, a high temperature (320 °C) and a prolonged reaction time (4 h) can provide sufficient energy to form hollow bimetallic Ni$_{2-x}$Mn$_x$P NCs.

Moreover, we also studied the influence of different Ni and Mn precursors as well as TOP concentrations (Fig. S3), where we found that the former has no significant influence on the hollow nanostructure of Ni$_{2-x}$Mn$_x$P NCs (Fig. S3a-d). However, the concentration of TOP plays a role in forming solid and hollow Ni$_{2-x}$Mn$_x$P NCs. When lower concentration of TOP (4 mM) was used during the reaction, solid Ni$_{2-x}$Mn$_x$P NCs with large size were obtained (Fig. S3e). The NCs size was further decreased when the large amounts of TOP were used (9 mM and 14 mM) (Fig. S3f and g), which follows similar trend to the reported literature [37]. In addition, hollowing of NCs begins with increase in TOP concentrations to 9 mM and complete formation of hollow Ni$_{2-x}$Mn$_x$P NCs is achieved when 14 mM TOP concentration was used. The corresponding PXRD patterns as shown in Fig. S3h illustrate the formation of single phase Ni$_{2-x}$Mn$_x$P NCs at higher TOP concentrations, whereas NCs synthesized with 5 mmol TOP concentration represent the initial stage of the formation of Ni$_{2-x}$Mn$_x$P NCs. We further synthesized Ni$_{2-x}$Mn$_x$P NCs using hot-injection method to see if the synthesis route affects the hollowing process of NCs. Interestingly, we found that the formation of hollow Ni$_{2-x}$Mn$_x$P NCs is independent of synthesis method employed (Fig. S3i-k). Thus, it is reasonable to conclude that the findings taken together show that Mn doping induces the Kirkendall effect in Ni$_2$P NCs, resulting in the formation of hollow NCs, while simultaneously emphasizing the importance of the carefully selecting reaction conditions that allow control over not only the phase of NCs, but also their size and morphology. We note that only one report is available on the nanoscale preparation of solid Mn-doped P-rich nickel phosphide, however the colloidal synthesis of hollow NCs and their detailed formation mechanisms have yet to be reported.

To get insights into the chemical states and further confirm the Mn doping, the X-ray photoelectron spectroscopy (XPS) measurements were performed on Ni$_2$P, Ni$_{1.8}$Mn$_{0.2}$P, Ni$_{1.6}$Mn$_{0.4}$P, and Ni$_{1.4}$Mn$_{0.6}$P NCs. The high-resolution survey spectra of Ni$_{1.4}$Mn$_{0.6}$P NCs (Fig. S4a) notably indicate the existence of Ni, Mn, and P, confirming the successful doping. As shown in Fig. 2**a**, the binding energy of Ni 2p$_{3/2}$ presented Ni-P at 851.9 eV for Ni$_2$P, which shifted to 853.05, 853.1, 852.8 eV for Ni$_{1.8}$Mn$_{0.2}$P, Ni$_{1.6}$Mn$_{0.4}$P, and Ni$_{1.4}$Mn$_{0.6}$P, respectively. Similarly, the binding energy of Mn 2p$_{3/2}$ shifted to 641.35, 641.2 and 640.6 eV for Ni$_{1.8}$Mn$_{0.2}$P, Ni$_{1.6}$Mn$_{0.4}$P, and Ni$_{1.4}$Mn$_{0.6}$P, respectively (Fig. 2**b**). Meanwhile, the binding energy of P 2p$_{3/2}$ in Ni$_2$P located at 130.8 eV

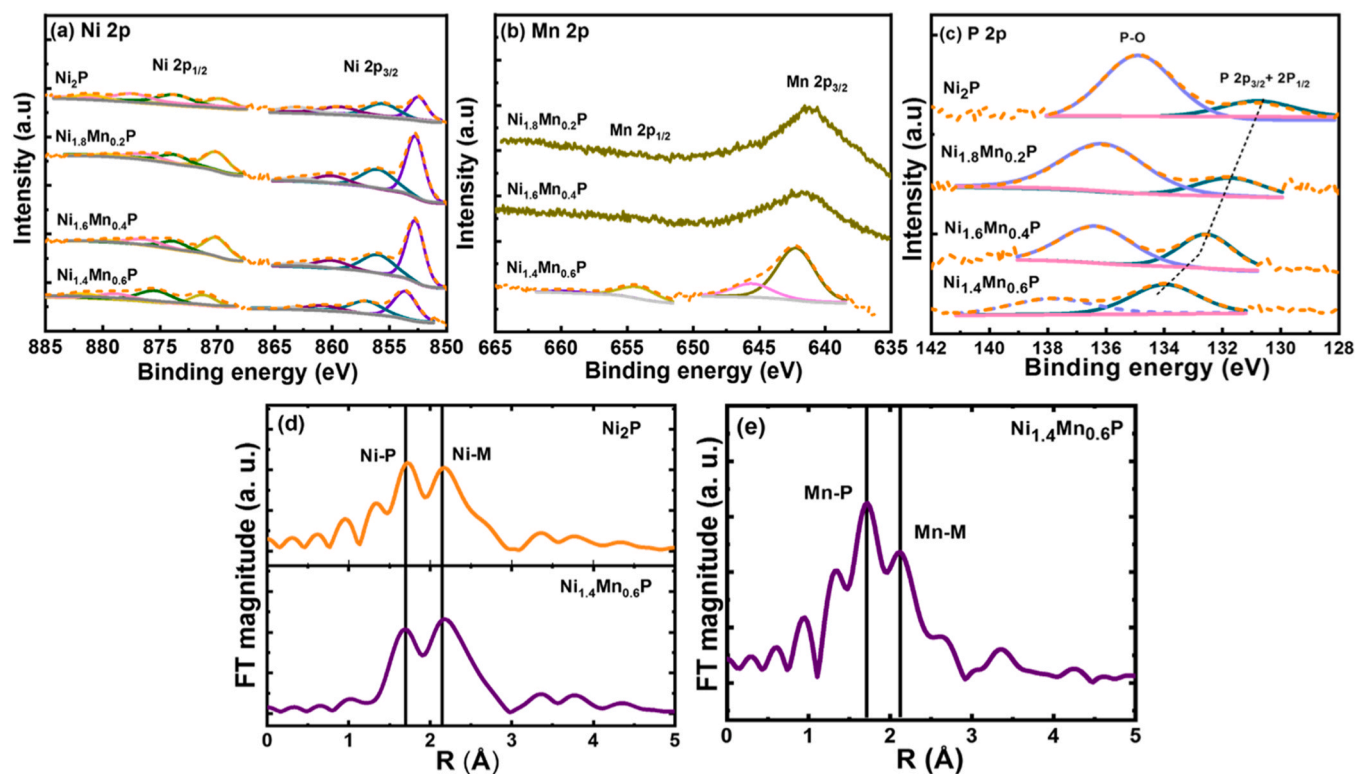**Fig. 2.** High-resolution XPS spectra of (a) Ni 2p, (b) Mn 2p and (c) P 2p for Ni_2P, $Ni_{1.8}Mn_{0.2}P$, $Ni_{1.6}Mn_{0.4}P$, and $Ni_{1.4}Mn_{0.6}P$ NCs. Fourier transforms of the (d) Ni K-edge spectra of Ni_2P and $Ni_{1.4}Mn_{0.6}P$ NCs, and (e) Mn K-edge EXAFS spectrum of $Ni_{1.4}Mn_{0.6}P$ NCs.

shifted to 131.9, 132.6 and 134 eV for $Ni_{1.8}Mn_{0.2}P$, $Ni_{1.6}Mn_{0.4}P$, and $Ni_{1.4}Mn_{0.6}P$, respectively (Fig. 2c). Additional peak at higher binding energy (134.4 ~ 137.7 eV) represents the satellite peaks and P^{5+} components oxidized from TOP. The Mn-doping concentration dependent binding energy changes is shown in Fig. S4b. The binding energy of Ni increases, while the binding energy of Mn decreases with increasing the Mn contents. The substitution of Ni atoms by Mn provides more electropositive Mn atoms surrounding each Ni atom. Due to the presence of next-nearest Mn adjacent atoms, the binding energy of Ni increases with an increase in Mn content up to x = 0.4 (for $Ni_{1.6}Mn_{0.4}P$ NCs) and subsequently decreases for higher Mn contents ($Ni_{1.4}Mn_{0.6}P$ NCs). It is possible that excess Mn atoms, while contributing to the overall structural orderliness, may reach a saturation point where further Mn incorporation leads to structural disruptions or defects. These disruptions could weaken the Ni-Mn bonds, resulting in the observed decrease in binding energy of Ni [51]. Similarly, the binding energy of P increases with increase in Mn contents. However, the binding energy of P $2p_{3/2}$ is substantially larger in $Ni_{1.4}Mn_{0.6}P$ than the Ni_2P. Based on the charge potential model [51], we propose that the positive shift of P $2p_{3/2}$ binding energy in $Ni_{1.4}Mn_{0.6}P$ is due to the intra-atomic effect. In addition, such significant shift in P $2p_{3/2}$ core level spectra could be attributed to the charge transfer effects, electronic structure modifications, surface effects and lattice strain induced by Mn doping [52]. To further shed a light on intra-atomic effect as well as to understand more details from the structural aspects after Mn-doping, the extended X-ray absorption fine structure (EXAFS) analysis was performed on Ni_2P and $Ni_{1.4}Mn_{0.6}P$. Fig. 2d and e shows the experimental χ(R) vs. R of Ni_2P and $Ni_{1.4}Mn_{0.6}P$ samples at Ni and Mn K-edges, respectively. Due to close atomic sizes of Ni and Mn and consistent crystals structure of $Ni_{2-x}Mn_xP$ over the composition range, the differentiating Ni and Mn while fitting the EXAFS was difficult. As shown in Fourier transform (FT) of Ni K edge (Fig. 2d), the two shells at 1.80 and 2.25 Å signify the distances of the Ni-P and Ni-M bonds in the P6¯2 m structure, respectively. The χ(R) of the Ni-P bond was larger than Ni-M bond in Ni_2P, whereas the χ(R)

of the Ni-P bond was smaller than the Ni-M bond for $Ni_{1.4}Mn_{0.6}P$. The Mn EXAFS also showed that the χ(R) of the Ni-P bond was larger than the Ni-M bond in the $Ni_{1.4}Mn_{0.6}P$. We further performed FT-EXAFS fitting to acquire more information on the coordination environment of Ni_2P and $Ni_{1.4}Mn_{0.6}P$ (Fig. S5). Table S3 displayed the structural parameters around Ni and Mn atoms by extracting from EXAFS data. Comparing with Ni_2P, the Ni-M coordination number in $Ni_{1.4}Mn_{0.6}P$ increases while the Ni-P coordination number decreases, suggesting that the doped Mn most possibly substitutes Ni sites. The low distortion level (i.e. $σ^2$, which represents the distortion degree of bond structures) for Ni-P bond in Ni_2P compared to $Ni_{1.4}Mn_{0.6}P$ indicates that the metal atoms surrounded the P atoms coherently. In contrast, the distortion level of Ni-M bond in Ni_2P was higher than in $Ni_{1.4}Mn_{0.6}P$, suggesting substantial distortions between Ni and adjacent metal atoms. The $Ni_{1.4}Mn_{0.6}P$, on the other hand, showed significant distortion in the Ni-P bond and a highly ordered Ni-M local structure. The Mn EXAFS fitting further reveals a similar tendency of $σ^2$ when Mn atoms are defined as center atoms. It has been revealed that the local structural distortions of the catalysts provide efficient active sites for electrochemical processes [52,53]. Therefore, we imply that the local distortion of Ni-P bond caused by the highly ordered Ni-M bond in $Ni_{1.4}Mn_{0.6}P$ enhances HER kinetics.

3.2. Investigations of HzOR and HER activities

The electrocatalytic HzOR and HER performances were evaluated using a typical three-electrode configuration with Ag/AgCl as a reference electrode and Ni foam loaded with catalyst as the counter electrode. At first, the electrocatalytic HzOR activities of $Ni_{2-x}Mn_xP$ (x = 0, 0.2, 0.4, 0.6) electrocatalysts were evaluated in 1.0 M KOH/0.5 M hydrazine electrolyte. Fig. 3a displays the linear sweep voltammetry (LSV) curves of Ni_2P, $Ni_{1.8}Mn_{0.2}P$, $Ni_{1.6}Mn_{0.4}P$, and $Ni_{1.4}Mn_{0.6}P$ electrocatalysts, which can intuitively demonstrate the superior electrocatalytic activity of $Ni_{1.4}Mn_{0.6}P$ electrocatalyst compared to other
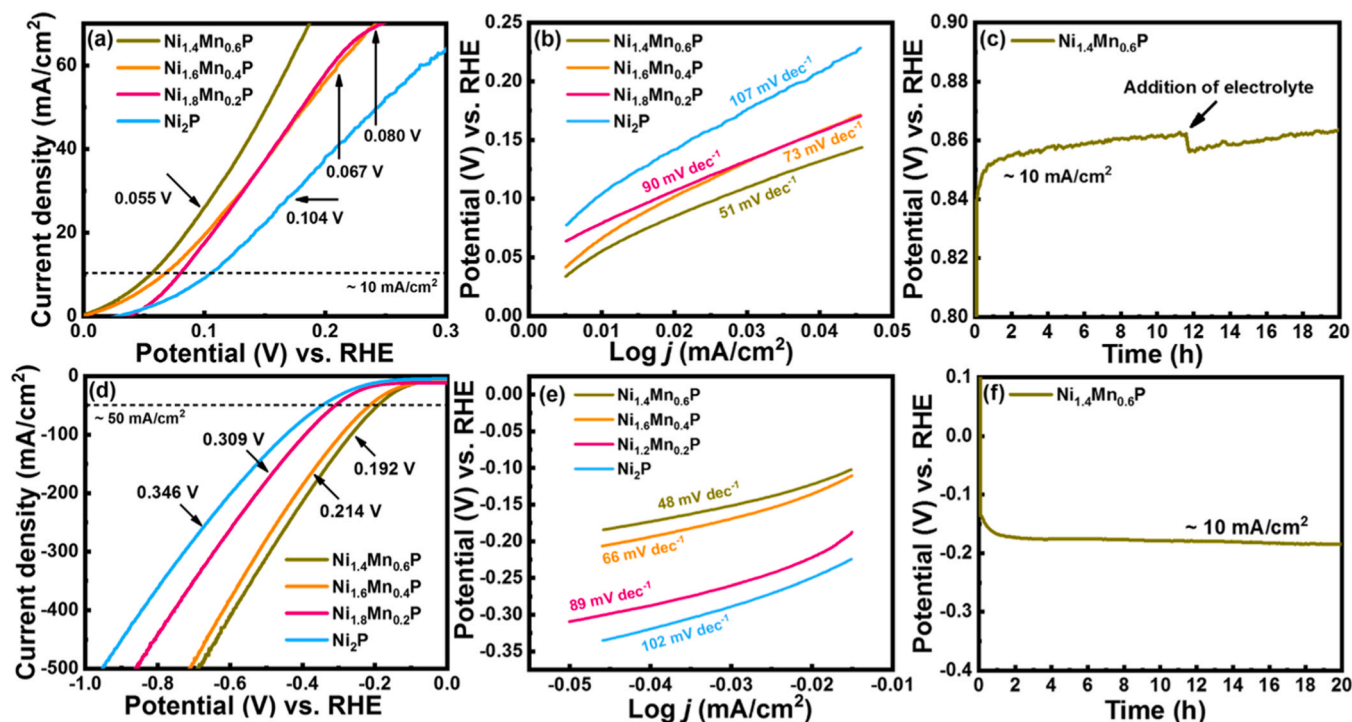
Fig. 3. (a) LSV curves and (b) corresponding tafel plots of $Ni_{2-x}Mn_xP$ NCs (x = 0, 0.2, 0.4, and 0.6) for HzOR. (c) Durability test of $Ni_{1.4}Mn_{0.6}P$ NCs for 20 h. (d) LSV curves and (e) corresponding Nyquist plots of $Ni_{2-x}Mn_xP$ NCs (x = 0, 0.2, 0.4, and 0.6) for HER. (f) Durability test of $Ni_{1.4}Mn_{0.6}P$ NCs for 20 h.

electrocatalysts. To be specific, the $Ni_{1.4}Mn_{0.6}P$ electrocatalyst needs low working potentials of 55 mV and 151 mV to achieve anodic current density of 10 and 50 mA/cm^2, which is excellent compared to bare Ni_2P, signifying the vitalness of Mn doping. To be noted, our hollow $Ni_{1.4}Mn_{0.6}P$ NCs-based electrocatalyst showed a comparable performance to most of the reported electrocatalysts and superior to powdered electrocatalysts. We further investigated the electrocatalytic activity of $Ni_{1.4}Mn_{0.6}P$ electrocatalyst in 1.0 M KOH electrolyte with different hydrazine concentrations (Fig. S6). Increasing the hydrazine concentration from 0.01 M to 0.5 M, a sharp rise in anodic current was observed, indicating the promising electrocatalytic activity of $Ni_{1.4}Mn_{0.6}P$ electrocatalyst toward HzOR (Fig. S6). The oxidation current was found to increase linearly with the added hydrazine, suggesting the potential of $Ni_{1.4}Mn_{0.6}P$ as an electrochemical sensor to detect hydrazine [14,23]. Besides, the corresponding Tafel slope of $Ni_{1.4}Mn_{0.6}P$ is 51 mV dec^{-1}, which is lower than that of $Ni_{1.6}Mn_{0.4}P$ (73 mV dec^{-1}), $Ni_{1.8}Mn_{0.2}P$ (90 mV dec^{-1}) and Ni_2P (107 mV dec^{-1}), suggesting the most favorable kinetics of $Ni_{1.4}Mn_{0.6}P$ electrocatalysts for HzOR (Fig. 3**b**). The electrochemical impedance spectroscopy (EIS) analyses were further conducted to understand the charge transfer kinetics that supports the above results, where the charge transfer resistance (R_{ct}) of $Ni_{1.4}Mn_{0.6}P$ electrocatalyst is relatively low than those of $Ni_{1.6}Mn_{0.4}P$, $Ni_{1.8}Mn_{0.2}P$ and Ni_2P electrocatalysts (Fig. S7). The electrochemically active surface area (ECSA) of $Ni_{1.4}Mn_{0.6}P$ electrocatalyst is estimated to be 7.91 cm^2, which is higher among the other electrocatalysts (Fig. S8). The calculated specific active surface area of the electrocatalyst using Brunauer-Emmett-Teller (BET) measurement is consistent with above results, where the $Ni_{1.4}Mn_{0.6}P$ electrocatalyst exhibits significantly higher active surface area of ~ 17.41 m^2 g^{-1} (Fig. S9a). To further assess the intrinsic activities of electrocatalysts, the mass activity and specific activity were evaluated by normalizing the LSV curves with mass loading and ECSAs, respectively (Fig. S9b and c). The $Ni_{1.4}Mn_{0.6}P$ electrocatalyst exhibits the mass activity of 0.044 A/mg, which is higher than $Ni_{1.6}Mn_{0.4}P$ (0.033 A/mg), $Ni_{1.8}Mn_{0.2}P$ (0.031 A/mg) and Ni_2P (0.021 A/mg) (Fig. S9d). Also, the $Ni_{1.4}Mn_{0.6}P$ electrocatalyst possesses the highest specific activity of 1.56 mA/cm^2 among other

electrocatalysts (Fig. S9d), confirming the superior catalytic activity of $Ni_{1.4}Mn_{0.6}P$ electrocatalysts towards HzOR. The durability of electrocatalyst is one of the critical factors for commercialization. Therefore, the long-term durability of $Ni_{1.4}Mn_{0.6}P$ was examined using chronopotentiometry test. Negligible change in the potential can be seen during the chronopotentiometric test for 20 h, demonstrating the excellent long-term durability of $Ni_{1.4}Mn_{0.6}P$ electrocatalyst (Fig. 3c).

The HER activities of the electrocatalysts were then evaluated in 1.0 M KOH electrolyte. The LSV curves (Fig. 3d) depict that the $Ni_{1.4}Mn_{0.6}P$ outperforms all other electrocatalysts and merely needs low overpotential of 192 mV to achieve current density of 50 mA/cm^2, which is much smaller than the $Ni_{1.6}Mn_{0.4}P$ (214 mV), $Ni_{1.8}Mn_{0.2}P$ (309 mV) and Ni_2P (346 mV). This remarkable HER performance of $Ni_{1.4}Mn_{0.6}P$ is superior/comparable to the recently reported non-precious and earth-abundant powdered electrocatalysts (Table S4). The Tafel slope of 48 mV dec^{-1} (Fig. 3e) and lower R_{ct} (Fig. S10) of $Ni_{1.4}Mn_{0.6}P$ electrocatalyst than those of $Ni_{1.6}Mn_{0.4}P$, $Ni_{1.8}Mn_{0.2}P$ and Ni_2P electrocatalysts offer a synergy towards favorable reaction kinetics for HER. Besides, the LSV curves were normalized by the mass loading and ECSAs of electrocatalysts to confirm their mass and specific activities (Fig. S11a-c). The plots (Fig. S11a and c) show the better mass activity of $Ni_{1.4}Mn_{0.6}P$ than that of $Ni_{1.6}Mn_{0.4}P$, $Ni_{1.8}Mn_{0.2}P$ and Ni_2P electrocatalysts, confirming the industrial advantage of $Ni_{1.4}Mn_{0.6}P$ as HER electrocatalyst. The ECSA-normalized LSV curves (Fig. S11b) show that the current density at an overpotential of 500 mV for $Ni_{1.4}Mn_{0.6}P$, $Ni_{1.6}Mn_{0.4}P$, $Ni_{1.8}Mn_{0.2}P$ and Ni_2P is 0.54, 0.482, 0.451 and 0.393 mA/cm^2, indicating that the superiority of $Ni_{1.4}Mn_{0.6}P$ for improving the HER activity among other electrocatalysts. To better understand the intrinsic activity towards HER, the turnover frequency (TOF) was calculated (Fig. S12). The TOF value of $Ni_{1.4}Mn_{0.6}P$ (1.531 S^{-1}) at overpotential of 200 mV, is relatively higher than other electrocatalysts, signifying the better intrinsic activity of $Ni_{1.4}Mn_{0.6}P$ toward HER. Moreover, the long-term durability test by a chronopotentiometric test further reveals that the negligible change in the potential after 20 h continuous test (Fig. 3f). Based on these multiple measurements, it is reasonable to state that the $Ni_{1.4}Mn_{0.6}P$ electrocatalyst exhibits the

excellent activity and outstanding durability for HER in alkaline condition.

3.3. Evaluation of $Ni_{1.4}Mn_{0.6}P$ as bifunctional electrocatalysts for HzOWS

Encouraged by the high activities and excellent stabilities of $Ni_{1.4}Mn_{0.6}P$ electrocatalyst for HzOR and HER, we further demonstrated its potential application as a bifunctional electrocatalyst (as cathode and anode) for HzOWS in a two-electrode electrolyzer (HzOWS unit, whose products are H_2 and N_2) using 1.0 M KOH/0.5 M hydrazine as an electrolyte. Considering the safety of the anodic N_2 and cathodic H_2 mixture and decreased solution resistance, the single-chamber, membrane-free electrolyzer was used in this study (See the Supplementary Movie 1 for its optical images). For comparison, the two-electrode system was also constructed for OER and HER (overall water splitting, OWS). The LSV curves (Fig. 4a) show the electrocatalytic activity of $Ni_{1.4}Mn_{0.6}P$ towards HzOWS and OWS in 1.0 M KOH/0.5 M hydrazine and 1.0 M KOH, respectively, in which it can be intuitively observed that the energy efficiency is significantly increased using hydrazine oxidation-assisted H_2 production. Specifically, $Ni_{1.4}Mn_{0.6}P$ electrocatalyst just needs an

ultralow cell voltage of 59 mV to reach 10 mA/cm^2, which is superior to recently reported values (Table S5). Notably, when compared the LSV curves of HzOWS and OWS, an obvious reduction in electric power can be observed using hydrazine oxidation-assisted H_2 production system (Fig. 4a). To be more specific, HzOWS unit only requires the cell voltages of 0.059 and 0.5 V to achieve the current density of 10 and 50 mA/cm^2 respectively, whereas much higher cell voltages of 1.45 V and 1.78 V for OWS systems, respectively. Besides, the HzOWS system also shows excellent stability, where a slight increase in current density can be seen during 20 h electrolysis at an applied cell voltage of 51 mV (Fig. 4b). The Faradic efficiency is further estimated to be ~ 98 % (Fig. S13a) for H_2 evolution in HzOWS system, which is slightly better than that of OWS system (94 %, (Fig. S13b), demonstrating higher electron utilization rate during electrolysis in HzOWS system.

Supplementary material related to this article can be found online at doi:10.1016/j.apcatb.2024.124165.

To further demonstrate the possible application of $Ni_{1.4}Mn_{0.6}P$ electrocatalyst, a proof-of-concept solar-energy-driven HzOWS cell was assembled by integrating commercial silicon photovoltaic (PV) device (power conversion efficiency of 29.3%, (Fig. S14) with the bifunctional $Ni_{1.4}Mn_{0.6}P$ (+) || $Ni_{1.4}Mn_{0.6}P$ (-) electrocatalyst (Fig. 4c). When tested
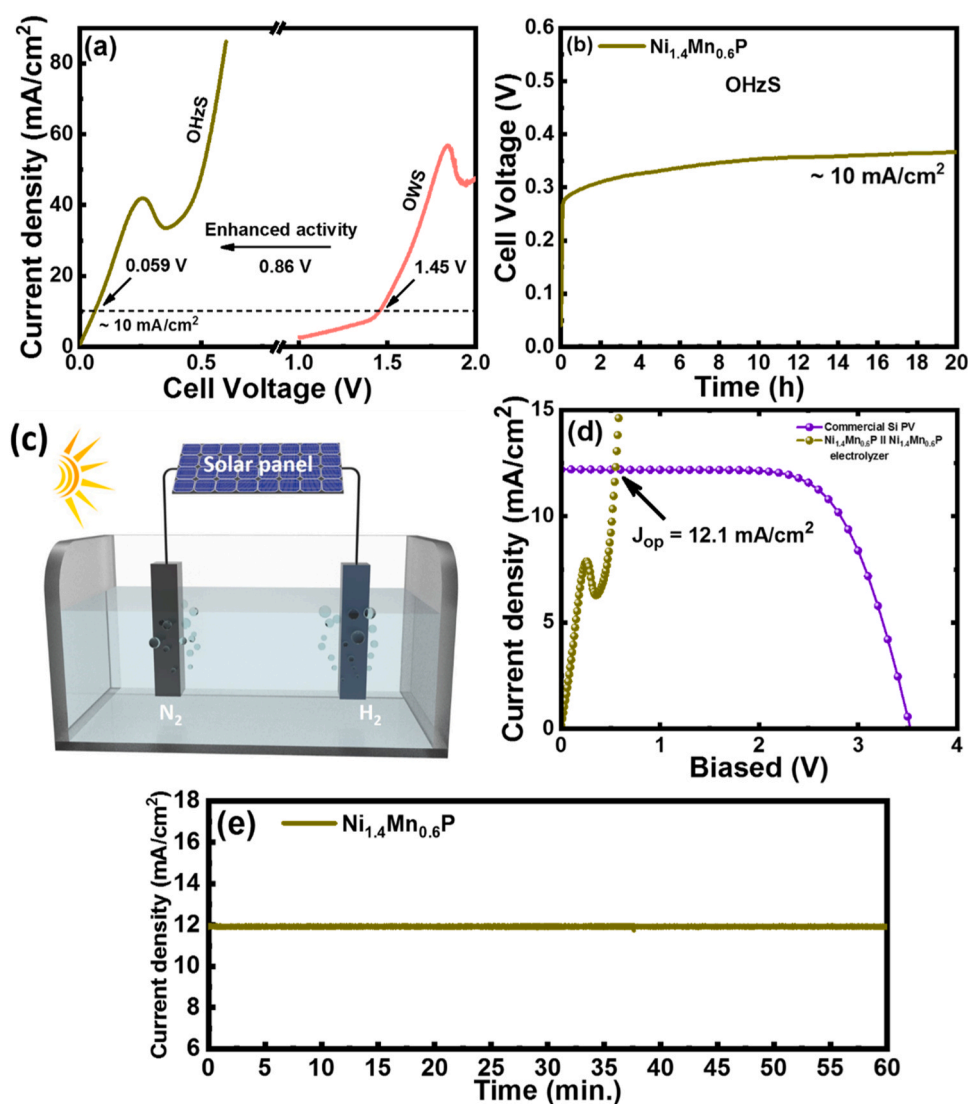

Fig. 4. (a) Comparison of LSV curves for HzOWS in 1.0 M KOH/0.5 M hydrazine and OWS in 1.0 M KOH using $Ni_{1.4}Mn_{0.6}P$ NCs as both the anode and cathode. (b) Durability test of HzOWS for 65 h. (c) Schematic representation of a reactor for solar-driven electrolysis. (d) Solar-to-hydrogen (STH) efficiency plot for HzOWS system. (e) Unbiased water splitting photocurrent measured for 60 min. in HzOWS system.

under natural sunlight conditions (Supplementary Movie 1) and under solar simulator (Supplementary Movie 2), H_2 and N_2 evolved continuously at the cathode and anode sides, respectively (Supplementary Movie 1 and 2 and Fig. S15). As revealed in Fig. 4d, the integrated device produced a very high current density of 12.1 mA/cm^2 that corresponds to a STH efficiency of ∼ 14.6% under 1 sun illumination, which is the comparable to the reported values to date for OWS and notably the first for solar-driven HzOWS system (Table S6). Moreover, this integrated device also retained almost similar photocurrent density for 1 h under continuous light illumination without any external voltage with vigorous gas bubble generation on both cathode and anode (Fig. 4e and Fig. S15c). In spite of breakthrough results and convenience of hydrazine as a liquid fuel at ordinary temperature over gaseous H_2 or carbon monoxide, high toxicity of hydrazine makes it challenging for large-scale applications. However, a detoxification technique, reported by Asazawa et al. [54], for fixing hydrazine would be safer since it bonds to carbonyl or amide groups in a non-toxic, stable, and recyclable polymer which can be released using water or aqueous KOH. This could be a relatively safe and promising strategy for large-scale applications of hydrazine-assisted H_2 production systems.

Supplementary material related to this article can be found online at doi:10.1016/j.apcatb.2024.124165.

3.4. Postcatalytic characterizations and DFT calculations

The post-catalytic samples were further characterized to investigate the possible structural changes and to understand the electrocatalytic activities of $Ni_{1.4}Mn_{0.6}P$ toward HzOR and HER. The TEM images (Fig. S16a and c) show no noticeable changes in the morphology and microstructure, including the hollow structure of $Ni_{1.4}Mn_{0.6}P$, whereas the EDS elemental mapping images (Fig. S16b and d) show even distribution of all elements, suggesting the structural robustness of the $Ni_{1.4}Mn_{0.6}P$ during the electrolysis. The XPS results (Fig. S17a-c) show unchanged binding energies of Ni 2p, Mn 2p and P 2p elements, further elucidating the stable surface chemical states of the $Ni_{1.4}Mn_{0.6}P$ NCs after/during the electrocatalytic processes. However, a slightly decreased peak intensity of the P-O peaks in P 2p spectra for the post-HzOR/HER samples is observed, possibly due to the dissolution of the phosphate under the alkaline conditions [55]. Altogether these results elucidate the structural robustness that efficiently facilitates the charge

transfer during the electrochemical processes, and thereby enhances the electrochemical activity as well as durability. Moreover, the preserved composition and phase concludes that the $Ni_{1.4}Mn_{0.6}P$ itself may act as the active species for both HzOR and HER.

To further reveal the possible origin of the better performance after Mn doping, DFT calculations were performed for the HzOR and HER processes. Generally, the HER process can be determined with three states such as an initial pair of H^+ and e^-, an intermediate of adsorbed H (H*) and the final product of 1/2 H_2, in which the free energy value of adsorbed H (ΔG_{H*}) is the critical descriptor for HER activity [46]. We performed DFT calculations to compute the free-energy of adsorbed H (ΔG_{H*}) on the Ni site of the undoped and Mn-doped Ni_2P surfaces. To model different concentrations of Mn dopants in Ni_2P, we replaced one, two and three Ni atoms in the subsurface layer by one, two and three Mn atoms, respectively (Fig. 5a-d). The ΔG_{H*} values are calculated to be −0.32 eV (the Ni site of Ni_2P) for the undoped case, while we obtained values of −0.20 eV, −0.15 eV, and −0.08 eV for the Ni_2P surface doped with one (1Mn-doped), two (2Mn-doped) and three Mn (3Mn-doped) atoms, respectively, as displayed in Fig. 5e and S18a. A close-to-thermoneutral value of −0.08 eV calculated for the 3Mn-doped Ni_2P compared to that of the pure Ni_2P (-0.32 eV), suggesting that Mn doping increased hydrogen adsorption and desorption, which is consistent with HER activity (Fig. 3d). Furthermore, the density of states (DOS) of 3Mn-doped Ni_2P at the Fermi level is slightly increased (Fig. S18b), implying that the enhanced electrical conductivity as a result of electronic modulation of Ni_2P after Mn doping boosts charge transfer kinetics and increases the number of active sites involved in the catalytic reaction.

Taking into account the fewer reports on the HzOR activity of Ni_2P-based electrocatalysts, it is then imperative to decipher the likely fundamental origins of the excellent HzOR activity of $Ni_{1.6}Mn_{0.4}P$ electrocatalyst compared to the undoped Ni_2P via DFT calculations. To this end, the HzOR reduction potential energy diagram on undoped and Mn-doped Ni_2P structures were calculated, in which the dehydrogenation of N_2H_4* to N_2H_3* is found to be the potential-determining step (PDS), as shown in Fig. 5f and S18c. The reaction barrier associated with the PDS was computed to be 1.09 eV on the undoped Ni_2P surface. Interestingly, we noticed that this reaction barrier decreased to 1.02, 1.05 and 1.02 eV on 1Mn, 2Mn and 3Mn-doped Ni_2P surfaces, indicating that the HzOR is expected to proceed faster on Mn-doped Ni_2P surfaces.
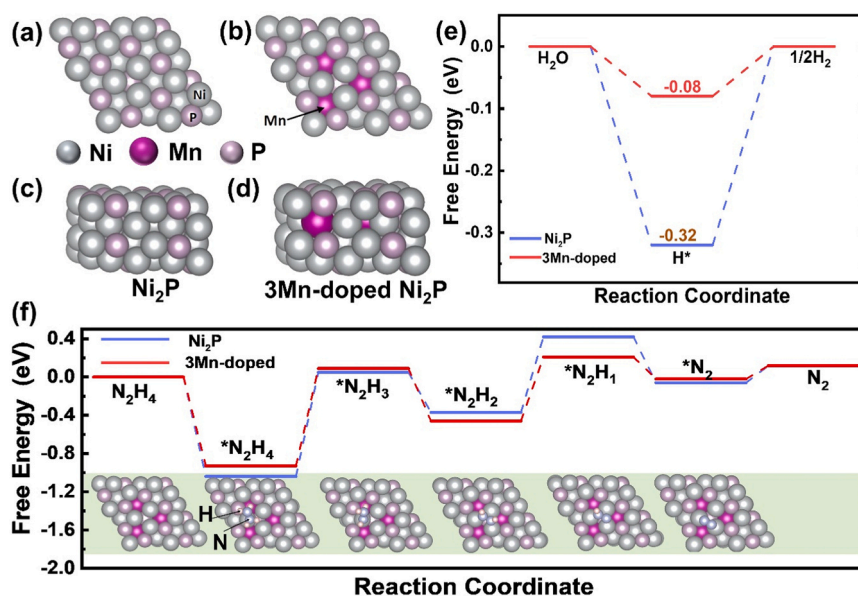

Fig. 5. (a-d) Top- and side-view of atomic structure models for Ni_2P and 3Mn-doped Ni_2P. (e) The free energy diagram of HER at the equilibrium potential for Ni_2P and 3Mn-doped Ni_2P, H* represents the intermediate adsorbed hydrogen. (f) The free energy profiles of HzOR for Ni_2P and 3Mn-doped Ni_2P and their corresponding stable configurations of the each adsorbed intermediates on the 3Mn-doped Ni_2P surfaces.

To understand the chemical origin for this reduction in barrier, we computed the Bader charges on the active Ni site present in the undoped and the 3Mn-doped Ni_2P surface model. We found that the electron density on the Ni atom in the 3Mn-doped model is larger by 0.025e- compared to the undoped case. Given that the N atom of the N_2H_4 molecule has a lone pair of electrons, the increased electron density on the Ni atom is expected to repel the N_2H_4 molecule and make the binding weaker, which is reflected in the energy diagram where $*N_2H_4$ and $*N_2H_3$ energy levels for the 3Mn-doped case lie higher than the levels obtained for the undoped case. Therefore, we expect the structural distortion (confirmed by the EXAFS (Fig. 2d and e) and the accompanying chemical changes imparted by Mn doping to favorably impact the HzOR process. The higher electron density on the Ni atom also helps explains the weaker interaction between H* and the catalyst. Taken together, these findings reveal that Mn doping could largely optimize electronic structure of Ni_2P, hence favorably facilitating the thermodynamics of both hydrogen adsorption in HER and dehydrogenation process in HzOR.

4. Conclusions

In summary, we have demonstrated the kinetically controlled synthesis of Mn-dopant induced hollow Ni_2P NCs via a simple heat-up approach, which exhibit a remarkable bifunctional electrocatalytic activity for both HzOR and HER in alkaline conditions. Concretely, it needs an ultralow working potential of 55 mV to reach 10 mA/cm^2 current density for HzOR in 1.0 M KOH/0.5 M hydrazine and can reach 50 mA/cm^2 at relatively small overpotential of 192 mV for HER in 1.0 M KOH, respectively. Importantly, the two-electrode HzOWS system using $Ni_{1.4}Mn_{0.6}P$ as both anode and cathode only demands a cell voltage of 59 mV to achieve distinct H_2 generation (10 mA/cm^2) and reach 50.4 mA/cm^2 current density at a small voltage of ~ 0.5 V. Inspired by the exceptional bifunctional performance, a proof-of-concept a solar-energy-driven HzOWS system was demonstrated using commercial Si PV device that showed a first notable STH efficiency of ~ 14.6 %. Experimental studies highlight the Mn induced hollowing in Ni_2P NCs via kirkendall effect, whereas the improved HzOR and HER activities are revealed by the theory calculations to originates from that the Mn doping not only makes ΔG_{H*} more thermoneutral but also decreases the free energy change of N_2H_4* on $Ni_{1.4}Mn_{0.6}P$.

CRediT authorship contribution statement

Umesh P. Suryawanshi: Writing – original draft, Visualization, Investigation, Formal analysis, Data curation, Conceptualization. **Uma V. Ghorpade:** Writing – review & editing, Supervision, Investigation, Formal analysis, Conceptualization. **Priyank V. Kumar:** Writing – review & editing, Visualization, Software, Methodology, Formal analysis. **Jun Sung Jang:** Writing – review & editing, Software, Resources, Project administration. **Mingrui He:** Writing – review & editing, Formal analysis. **Hong Jae Shim:** Writing – review & editing, Software, Resources. **Hyo Rim Jung:** Software, Resources, Formal analysis. **Mahesh P. Suryawanshi:** Writing – review & editing, Visualization, Supervision, Funding acquisition, Project administration, Investigation, Formal analysis, Data curation, Conceptualization. **Jin Hyeok Kim:** Writing – review & editing, Validation, Supervision, Resources, Project administration, Investigation, Funding acquisition.

Declaration of Competing Interest

The authors declare that they have no known competing financial interests or personal relationships that could have appeared to influence the work reported in this paper.

Data availability

Data will be made available on request.

Appendix A. Supporting information

Supplementary data associated with this article can be found in the online version at doi:10.1016/j.apcatb.2024.124165.

References

[1] M.P. Suryawanshi, U.V. Ghorpade, C.Y. Toe, U.P. Suryawanshi, M. He, D. Zhang, J. S. Jang, S.W. Shin, J.H. Kim, X. Hao, R. Amal, Earth-abundant photoelectrodes for water splitting and alternate oxidation reactions: recent advances and future perspectives, Prog. Mater. Sci. 134 (2023) 101073.

[2] I. Roger, M.A. Shipman, M.D. Symes, Earth-abundant catalysts for electrochemical and photoelectrochemical water splitting, Nat. Rev. Chem. 1 (2017) 1–13.

[3] M.P. Suryawanshi, U.V. Ghorpade, S.W. Shin, U.P. Suryawanshi, H.J. Shim, S. H. Kang, J.H. Kim, Facile, room temperature, electroless deposited (Fe1−x,Mnx) OOH nanosheets as advanced catalysts: the role of Mn incorporation, Small 14 (2018) 1801226.

[4] H. Zhang, X. Li, A. Hähnel, V. Naumann, C. Lin, S. Azimi, S.L. Schweizer, A. W. Maijenburg, R.B. Wehrspohn, Bifunctional heterostructure assembly of NiFe LDH nanosheets on NiCoP nanowires for highly efficient and stable overall water splitting, Adv. Funct. Mater. 28 (2018) 1706847.

[5] U.P. Suryawanshi, U.V. Ghorpade, D.M. Lee, M. He, S.W. Shin, P.V. Kumar, J. S. Jang, H.R. Jung, M.P. Suryawanshi, J.H. Kim, Colloidal Ni2P nanocrystals encapsulated in heteroatom-doped graphene nanosheets: a synergy of 0D@ 2D heterostructure toward overall water splitting, Chem. Mater. 33 (2020) 234–245.

[6] L. Dai, Q. Qin, X. Zhao, C. Xu, C. Hu, S. Mo, Y.O. Wang, S. Lin, Z. Tang, N. Zheng, Electrochemical partial reforming of ethanol into ethyl acetate using ultrathin Co3O4 nanosheets as a highly selective anode catalyst, ACS Cent. Sci. 2 (2016) 538–544.

[7] M.A. Gaikwad, V.V. Burungale, D.B. Malavekar, U.V. Ghorpade, U.P. Suryawanshi, S. jang, X. Guo, S.W. Shin, J.S. Ha, M.P. Suryawanshi, J.H. Kim, Self-supported Fe-based nanostructured electrocatalysts for water splitting and selective oxidation reactions: past, present, and future, Adv. Energy Mater. 15 (2024) 2303730.

[8] S. Chen, J. Duan, A. Vasileff, S.Z. Qiao, Size fractionation of two-dimensional sub-nanometer thin manganese dioxide crystals towards superior urea electrocatalytic conversion, Angew. Chem. 128 (2016) 3868–3872.

[9] U.P. Suryawanshi, U.V. Ghorpade, J.A. Yuwono, P.V. Kumar, M.A. Gaikwad, S. W. Shin, J.S. Jang, H.R. Jung, M.P. Suryawanshi, J.H. Kim, Cr-dopant induced crystal orientation and shape modulation in Ni2P nanocrystals for improving electrosynthesis of methanol to formate coupled with hydrogen production, J. Mater. Chem. A (2024), https://doi.org/10.1039/D4TA01147C.

[10] J.Y. Zhang, H. Wang, Y. Tian, Y. Yan, Q. Xue, T. He, H. Liu, C. Wang, Y. Chen, B. Y. Xia, Anodic hydrazine oxidation assists energy-efficient hydrogen evolution over a bifunctional cobalt perselenide nanosheet electrode, Angew. Chem. Int. Ed. 57 (2018) 7649–7653.

[11] M.A. Gaikwad, U.P. Suryawanshi, U.V. Ghorpade, J.S. Jang, M.P. Suryawanshi, J. H. Kim, Emerging surface, bulk, and interface engineering strategies on BiVO4 for photoelectrochemical water splitting, Small 18 (2022) 2105084.

[12] C. Huang, Y. Huang, C. Liu, Y. Yu, B. Zhang, Integrating hydrogen production with aqueous selective semi-dehydrogenation of tetrahydroisoquinolines over a Ni2P bifunctional electrode, Angew. Chem. 131 (2019) 12142–12145.

[13] B. You, N. Jiang, X. Liu, Y. Sun, Simultaneous H2 generation and biomass upgrading in water by an efficient noble-metal-free bifunctional electrocatalyst, Angew. Chem. Int. Ed. 55 (2016) 9913–9917.

[14] C. Tang, R. Zhang, W. Lu, Z. Wang, D. Liu, S. Hao, G. Du, A.M. Asiri, X. Sun, Energy-saving electrolytic hydrogen generation: Ni2P nanoarray as a high-performance non-noble-metal electrocatalyst, Angew. Chem. Int. Ed. 56 (2017) 842–846.

[15] L.-S. Wu, X.-P. Wen, H. Wen, H.-B. Dai, P. Wang, Palladium decorated porous nickel having enhanced electrocatalytic performance for hydrazine oxidation, J. Power Sources 412 (2019) 71–77.

[16] A. Landman, H. Dotan, G.E. Shter, M. Wullenkord, A. Houaijia, A. Maljusch, G. S. Grader, A. Rothschild, Photoelectrochemical water splitting in separate oxygen and hydrogen cells, Nat. Mater. 16 (2017) 646–651.

[17] Y. Zheng, Y. Jiao, Y. Zhu, L.H. Li, Y. Han, Y. Chen, A. Du, M. Jaroniec, S.Z. Qiao, Hydrogen evolution by a metal-free electrocatalyst, Nat. Commun. 5 (2014) 1–8.

[18] M.P. Surawanshi, U.V. Ghorpade, S.W. Shin, U.P. Suryawanshi, E. Jo, J.H. Kim, Hierarchically coupled Ni: FeOOH nanosheets on 3D N-doped graphite foam as self-supported electrocatalysts for efficient and durable water oxidation, ACS Catal. 9 (2019) 5025–5034.

[19] M. Liu, R. Zhang, L. Zhang, D. Liu, S. Hao, G. Du, A.M. Asiri, R. Kong, X. Sun, Energy-efficient electrolytic hydrogen generation using a Cu$_3$P nanoarray as a bifunctional catalyst for hydrazine oxidation and water reduction, Inorg. Chem. Front. 4 (2017) 420–423.

[20] Y. Gu, S. Chen, J. Ren, Y.A. Jia, C. Chen, S. Komarneni, D. Yang, X. Yao, Electronic structure tuning in Ni$_3$FeN/r-GO aerogel toward bifunctional electrocatalyst for overall water splitting, ACS Nano 12 (2018) 245–253.

[21] Z. Wang, L. Xu, F. Huang, L. Qu, J. Li, K.A. Owusu, Z. Liu, Z. Lin, B. Xiang, X. Liu, K. Zhao, X. Liao, W. Yang, Y.-B. Cheng, L. Mai, Copper–nickel nitride nanosheets as efficient bifunctional catalysts for hydrazine-assisted electrolytic hydrogen production, Adv. Energy Mater. 9 (2019) 1900390.

[22] Y. Zhao, N. Jia, X.-R. Wu, F.-M. Li, P. Chen, P.-J. Jin, S. Yin, Y. Chen, Rhodium phosphide ultrathin nanosheets for hydrazine oxidation boosted electrochemical water splitting, Appl. Catal. B 270 (2020) 118880.

[23] Y. Li, J. Zhang, Y. Liu, Q. Qian, Z. Li, Y. Zhu, G. Zhang, Partially exposed RuP$_2$ surface in hybrid structure endows its bifunctionality for hydrazine oxidation and hydrogen evolution catalysis, Sci. Adv. 6 (2020) eabb4197.

[24] J. Su, J. Zhou, L. Wang, C. Liu, Y. Chen, Synthesis and application of transition metal phosphides as electrocatalyst for water splitting, Science 62 (2017) 633–644.

[25] H. Li, Q. Li, P. Wen, T.B. Williams, S. Adhikari, C. Dun, C. Lu, D. Itanze, L. Jiang, D. L. Carroll, Colloidal cobalt phosphide nanocrystals as trifunctional electrocatalysts for overall water splitting powered by a zinc–air battery, Adv. Mater. 30 (2018) 1705796.

[26] J. Yang, D. Guo, S. Zhao, Y. Lin, R. Yang, D. Xu, N. Shi, X. Zhang, L. Lu, Y.Q. Lan, Cobalt phosphides nanocrystals encapsulated by P-doped carbon and married with P-doped graphene for overall water splitting, Small 15 (2019) 1804546.

[27] X. Liu, Y. Zhao, X. Yang, Q. Liu, X. Yu, Y. Li, H. Tang, T. Zhang, Porous Ni5P4 as a promising cocatalysts for boosting the photocatalytic hydrogen evolution reaction performance, Appl. Catal. B: Environ. 275 (2020) 119144.

[28] J. Chen, Q. Long, K. Xiao, T. Ouyang, N. Li, S. Ye, Z.-Q. Liu, Vertically-interlaced NiFeP/MXene electrocatalysts with tunable electronic structure for high-efficiency oxygen evolution reaction, Sci. Bull. 66 (2021) 1063–1072.

[29] J. Liang, F. Ma, S. Hwang, X. Wang, J. Sokolowski, Q. Li, G. Wu, D. Su, Atomic arrangement engineering of metallic nanocrystals for energy-conversion electrocatalysis, Joule 3 (2019) 956–991.

[30] M.H. Naveen, R. Khan, J.H. Bang, Gold nanoclusters as electrocatalysts: atomic level understanding from fundamentals to applications, Chem. Mater. 33 (2021) 7595–7612.

[31] T. Reier, Z. Pawolek, S. Cherevko, M. Bruns, T. Jones, D. Teschner, Sr Selve, A. Bergmann, H.N. Nong, R. Schlögl, Molecular insight in structure and activity of highly efficient, low-Ir Ir–Ni oxide catalysts for electrochemical water splitting (OER), J. Am. Chem. Soc. 137 (2015) 13031–13040.

[32] V.R. Stamenkovic, B.S. Mun, M. Arenz, K.J. Mayrhofer, C.A. Lucas, G. Wang, P. N. Ross, N.M. Markovic, Trends in electrocatalysis on extended and nanoscale Pt-bimetallic alloy surfaces, Nat. Mater. 6 (2007) 241–247.

[33] L. Yu, B.Y. Xia, X. Wang, X.W. Lou, General formation of M–MoS$_3$ (M= Co, Ni) hollow structures with enhanced electrocatalytic activity for hydrogen evolution, Adv. Mater. 28 (2016) 92–97.

[34] L. Yu, J.F. Yang, B.Y. Guan, Y. Lu, X.W. Lou, Hierarchical hollow nanoprisms based on ultrathin Ni-Fe layered double hydroxide nanosheets with enhanced electrocatalytic activity towards oxygen evolution, Angew. Chem. Inter. Ed. 57 (2018) 172–176.

[35] Y. Chen, Z. Li, Y. Zhu, D. Sun, X. Liu, L. Xu, Y. Tang, Atomic Fe dispersed on N-doped carbon hollow nanospheres for high-efficiency electrocatalytic oxygen reduction, Adv. Mater. 31 (2019) 1806312.

[36] A.E. Henkes, Y. Vasquez, R.E. Schaak, Converting metals into phosphides: a general strategy for the synthesis of metal phosphide nanocrystals, J. Am. Chem. Soc. 129 (2007) 1896–1897.

[37] J. Wang, A.C. Johnston-Peck, J.B. Tracy, Nickel phosphide nanoparticles with hollow, solid, and amorphous structures, Chem. Mater. 21 (2009) 4462–4467.

[38] G. Kresse, J. Hafner, Ab initio molecular-dynamics simulation of the liquid-metal–amorphous-semiconductor transition in germanium, Phys. Rev. B 49 (1994) 14251.

[39] G. Kresse, J. Furthmuller, Efficient iterative schemes for ab initio total-energy calculations using a plane-wave basis set, Phys. Rev. B 54 (1996) 11169.

[40] G. Kresse, D. Joubert, From ultrasoft pseudopotentials to the projector augmented-wave method, Phys. Rev. B 59 (1999) 1758.

[41] J.P. Perdew, K. Burke, M. Ernzerhof, Generalized gradient approximation made simple, Phys. Rev. Lett. 77 (1996) 3865.

[42] J.K. Nørskov, J. Rossmeisl, A. Logadottir, L. Lindqvist, J.R. Kitchin, T. Bligaard, H. Jónsson, Origin of the overpotential for oxygen reduction at a fuel-cell cathode, J. Phys. Chem. B 108 (2004) 17886.

[43] A.A. Peterson, F. Abild-Pedersen, F. Studt, J. Rossmeisl, J.K. Nørskov, How copper catalyzes the electroreduction of carbon dioxide into hydrocarbon fuels, Energy Environ. Sci. 3 (2010) 1311.

[44] H.-W. Man, C.-S. Tsang, M.M.-J. Li, J. Mo, B. Huang, L.Y.S. Lee, Y.-C. Leung, K.-Y. Wong, S.C.E. Tsang, Transition metal-doped nickel phosphide nanoparticles as electro-and photocatalysts for hydrogen generation reactions, Appl. Catal. B. 242 (2019) 186–193.

[45] D. Li, H. Baydoun, C.N. Verani, S.L. Brock, Efficient water oxidation using CoMnP nanoparticles, J. Am. Chem. Soc. 138 (2016) 4006–4009.

[46] J.X. Wang, C. Ma, Y. Choi, D. Su, Y. Zhu, P. Liu, R. Si, M.B. Vukmirovic, Y. Zhang, R.R. Adzic, Kirkendall effect and lattice contraction in nanocatalysts: a new strategy to enhance sustainable activity, J. Am. Chem. Soc. 133 (2011) 13551–13557.

[47] S.W. Chee, Z.M. Wong, Z. Baraissov, S.F. Tan, T.L. Tan, U. Mirsaidov, Interface-mediated Kirkendall effect and nanoscale void migration in bimetallic nanoparticles during interdiffusion, Nat. Commun. 10 (2019) 1–8.

[48] B.D. Anderson, J.B. Tracy, Nanoparticle conversion chemistry: Kirkendall effect, galvanic exchange, and anion exchange, Nanoscale 6 (2014) 12195–12216.

[49] H. Tianou, W. Wang, X. Yang, Z. Cao, Q. Kuang, Z. Wang, Z. Shan, M. Jin, Y. Yin, Inflating hollow nanocrystals through a repeated Kirkendall cavitation process, Nat. Commun. 8 (2017) 1–9.

[50] R.-K. Chiang, R.-T. Chiang, Formation of hollow Ni$_2$P nanoparticles based on the nanoscale Kirkendall effect, Inorg. Chem. 46 (2007) 369–371.

[51] P.E. Blanchard, A.P. Grosvenor, R.G. Cavell, A. Mar, Effects of metal substitution in transition-metal phosphides (Ni$_{1-x}$M$'_x$)$_2$P (M'= Cr, Fe, Co) studied by X-ray photoelectron and absorption spectroscopy, J. Mater. Chem. 19 (2009) 6015–6022.

[52] Y. Sun, H. Cheng, S. Gao, Z. Sun, Q. Liu, Q. Liu, F. Lei, T. Yao, J. He, S. Wei, Freestanding tin disulfide single-layers realizing efficient visible-light water splitting, Angew. Chem. Inter. Ed. 51 (2012) 8727–8731.

[53] Y. Sun, Q. Liu, S. Gao, H. Cheng, F. Lei, Z. Sun, Y. Jiang, H. Su, S. Wei, Y. Xie, Pits confined in ultrathin cerium (IV) oxide for studying catalytic centers in carbon monoxide oxidation, Nat. Commun. 4 (2013) 1–8.

[54] K. Asazawa, K. Yamada, H. Tanaka, A. Oka, M. Taniguchi, T. Kobayashi, A platinum-free zero-carbon-emission easy fuelling direct hydrazine fuel cell for vehicles, Angew. Chem. 119 (2007) 8170–8173.

[55] N. Jiang, B. You, M. Sheng, Y. Sun, Electrodeposited cobalt-phosphorous-derived films as competent bifunctional catalysts for overall water splitting, Angew. Chem. 127 (2015) 6349–6352.